

## Magnetic-field-induced structural transitions in a ferrofluid emulsion

Mark Ivey, Jing Liu, Yun Zhu, and Serge Cutillas

*Department of Physics and Astronomy, California State University, Long Beach, California 90840*  
(Received 25 February 1999; revised manuscript received 1 June 2000; published 21 December 2000)

A ferrofluid emulsion, subjected to a slowly increasing magnetic field, exhibits a complicated structural behavior: a gas of Brownian particles changes to columnar solid structures due to induced dipole interaction. Two transition (intermediate) structural regimes are observed: (i) randomly distributed chains and particles and (ii) distinct thin columns and randomly distributed chains and particles. Three structural transition magnetic fields are found, one marking each structural transition, from the initial to the final structural regime. A structural diagram of the structural transition magnetic fields,  $H_C$ , versus particle volume fractions,  $\phi$ , is constructed experimentally. Theoretical models of scaling calculations, based upon the dominant magnetic interaction in each structural regime, give the three structural transition magnetic-field relations as  $H_{C1} \propto \phi^{-1/2}$ ,  $H_{C2} \propto \phi^{-1/4}$ , and  $H_{C3} \propto (\phi^\gamma/G^2)\exp(\pi G/\phi^{\gamma/2})$ , where  $\gamma=0.39$  and  $G=0.29$  for our sample. The final end shape of columns and the relative position between columns show that the end-end repulsion between chains is important in the structural formation.

DOI: 10.1103/PhysRevE.63.011403

PACS number(s): 82.70.Gg, 61.90.+d, 64.90.+b

### I. INTRODUCTION

Colloids exhibit a rich and highly varied phase and structural behavior. Depending on the interaction between the colloidal particles, the colloid can exhibit liquid, crystal, and glass phases. Many studies have been done in the past on the phase behavior of colloids with isotropic interactions, such as hard-sphere and Coulomb interactions [1–4]. These studies have led to the understanding of many macroscopic properties of the colloidal system, such as shear thinning and thickening. In the case of anisotropic interaction between colloidal particles, for example in a dipolar interaction, the phase behavior has received much less attention.

Two types of dipolar interactions in colloids have been studied so far: electric and magnetic. When an electric (or a magnetic) field is applied to a colloid in which the electric (or magnetic) permeability of the particle is mismatched with the fluid, an electric (or a magnetic) dipole is induced in each particle. The induced dipoles interact with one another, changing the structure of the colloids and causing a gas-solid or liquid-solid structural transition. These induced structures dramatically change the rheological properties of the fluids from liquid to solid, leading to many technological applications, hence these fluids are called electrorheological (ER) [or magnetorheological (MR)] fluids. While ER fluids have been studied for more than four decades and MR fluids for some years [5,6], the interaction mechanisms and the resulting equilibrium solid structures have only recently been explored in detail and are only beginning to be understood [7–11]. The complete phase and structural behavior and detailed transition process are still not fully understood.

A few studies have dealt with the field-induced phase and structural behavior in dipolar colloids, but different results have been reported. Sano and Doi theoretically predict that in ferrofluids the magnetic field induces a gas-liquid phase transition, with a single critical field [12]. Recent numerical simulations of ER fluids by Tao suggest that an electric field induces gas-liquid and liquid-solid phase transitions with two critical fields [13,14]. In ER fluids, although the final struc-

ture of a body-centered-tetragonal (BCT) lattice has been mapped out beautifully [15], only the initial stage of the phase transition, that of random particles to single chains, has been studied experimentally [16].

In MR fluids, two groups have studied the same polydisperse, density-mismatched system—polystyrene magnetic colloids—and they find different relationships between the magnetic field,  $H$ , and particle volume fraction,  $\phi$ : Hwang *et al.* found a two-transition process involving two critical fields  $H_{C1} \propto \phi^{-1/4}$  and  $H_{C2} \propto \phi^{-1/2}$  for a thin sample cell but no current theory can explain the results [17]; Lemaire *et al.* found a liquid-solid phase transition with a single critical field  $H_{C1} \propto \phi$  [9]. A recent work from the second group [18] shows that two critical fields exist for the transition classified as gas to liquid, where the first critical field is independent of  $\phi$  and the second critical field shows a “well”-like curve that cannot be explained by a simple first-order phase-transition model. As already noted, a complete picture of the field-induced phase and structural behavior in dipolar colloids has yet to be understood.

In this paper, we report a systematic study of the detailed behavior of magnetic-field-induced structural transitions in a model MR fluid, ferrofluid emulsion where the particle density is closely matched with the suspending liquid to prevent quick sedimentation and the particle size has a much narrower distribution than polystyrene magnetic colloids. Measurements of light transmission through the emulsion as a function of an externally applied magnetic field are used as the primary means of studying the structural transitions. Experimentally, we find four structural regimes: (i) randomly distributed particles (gas); (ii) coexistence of particles and randomly distributed short chains with random chain length (“nematic-liquid-crystal-like”); (iii) coexistence of particles, chains, and columns (liquid); and (iv) separated columns (solid). The entire structural transition process is divided by three structural transition magnetic fields, each one determined by identifying where a significant structural change occurs as determined by changes in the light transmission. A structural diagram of the structural transition magnetic fields,

$H_C$ , versus particle volume fractions,  $\phi$ , is constructed experimentally. Theoretical models of scaling calculations, based upon the dominant magnetic interaction in each structural regime, successfully explain all of the data, giving the three structural transition magnetic-field relations as  $H_{C1} \propto \phi^{-1/2}$ ,  $H_{C2} \propto \phi^{-1/4}$ , and  $H_{C3} \propto (\phi^\gamma/G^2)\exp(\pi G/\phi^{\gamma/2})$ , where  $\gamma=0.39$  and  $G=0.29$  for our sample.  $H_{C3}$  shows a complicated behavior where two particle volume fraction dependences are seen for the same structural transition magnetic field and  $\gamma$  and  $G$  are constants that reflect the detailed structure inside a column.

The long-range dipole-dipole interaction is responsible for the first structural transition: particles forming dimers or short chains. In the second structural transition, in which the center of each column is formed when long chains reach the boundaries of the sample cell acting as nuclei for short chains to coalesce, the monopole repulsion between ends of neighboring long chains sets the positions of the columnar structures. The short-range direct interaction between chains is responsible for the third structural transition: tightening of each loosely bound column. The final shape of the ends of the columns and the relative position between columns show that the end-end repulsion between chains is important in the structural formation.

It should be noted that parts of this paper—the transmission measurements and the main part of the structural transition theory—were previously presented in an earlier publication [5,19] as conference proceedings. In this paper, we have expanded the data, the discussion, and the theory and have revised the  $H_{C1}$  and  $H_{C3}$  data based upon improved criteria. These revisions can be seen most notably in the structural transition diagram that is presented later in this paper.

## II. FERROFLUID EMULSION PREPARATION AND PROPERTIES

### A. Emulsion preparation

In this study, a kerosene-based ferrofluid is used to make oil-in-water emulsions obtained by employing techniques established by Bibette [20,21]. The ferrofluid consists of 6.2% by volume of  $\text{Fe}_3\text{O}_4$  grains that have an average diameter of approximately 14 nm and are coated by oleic acid. The ferrofluid droplets are stabilized with 0.015 mol/l sodium dodecyl sulfate (SDS) surfactant, which is approximately twice the critical micellar concentration of 0.008 mol/l [21,22]. Once a crude oil-in-water emulsion is prepared, it is highly polydisperse, i.e., it contains a wide range of oil droplet sizes. A fractionated crystallization process involving attractive depletion interaction is used to separate the different sized droplets from one another [21]. Repeatedly applying this process results in a number of subsets of the original crude emulsion, each with a narrow droplet size distribution, which are used for experimentation.

The primary ferrofluid emulsion used in this study, unless mentioned otherwise, had a droplet diameter of 0.3  $\mu\text{m}$  and a standard deviation of 35%, which were determined by a dynamic light-scattering technique through measurement of the droplet diffusion coefficient in a low concentration [23]. The

emulsion droplet concentration is kept low (<5%) to enhance a long shelf life (greater than three months). Other concentrations were generated by adding or removing an appropriate amount of the water/SDS solution from the extracted base emulsion.

### B. Magnetic properties of ferrofluid emulsions

Each  $\text{Fe}_3\text{O}_4$  magnetite grain inside an emulsion droplet corresponds to a single magnetic domain and will, therefore, have a permanent dipole moment. In the absence of an externally applied magnetic field, the magnetic dipoles of the  $\text{Fe}_3\text{O}_4$  magnetite grains are randomly oriented in each droplet due to thermal motion at room temperature, thereby giving each ferrofluid droplet a zero net magnetic dipole moment. The ferrofluid droplets behave as hard spheres for droplet separation distances of 50 Å or larger [22,24]. This distance is set by the screened Coulomb interaction between charged SDS modules on the surface of droplets when they overlap. SDS is a surfactant with each molecule being approximately 20 Å in radius and consisting of a polar sulfate head (hydrophilic) and a nonpolar hydrocarbon tail (hydrophobic). When dissolved into water, the SDS molecules disassociate causing the polar sulfate head to become negatively charged [25]. The SDS molecules then arrange themselves both on the surface of oil droplets and into micelles so that exposure of the tail to the water is minimized, thereby minimizing the free energy [25]. If two droplets come near to one another, each droplet coated by charged SDS will experience a repulsive force due to static Coulomb interaction [24]. This repulsion will prevent the coalescence of the ferrofluid droplets against Van der Waal's attractive energy and maintain the distribution of the droplet sizes. The screening of droplet surface charges by cations in the water makes the Coulomb interaction very short-ranged. Because of the large surface tension and osmotic pressure for this size of droplet, we expect that the droplets experience no deformation for externally applied magnetic fields up to 360 G. This was verified by direct observation, using optical microscopy, of an 8- $\mu\text{m}$  droplet inside a ferrofluid emulsion of 0.3- $\mu\text{m}$  average droplet size, where it was observed that the large droplet experienced only an 8% deformation. Hence, we may neglect any deformation that might occur in smaller sized droplets, such as those in our primary ferrofluid emulsion.

When an external magnetic field is applied, a magnetic dipole moment is induced in each droplet by aligning the  $\text{Fe}_3\text{O}_4$  magnetite grains partially with the magnetic field. This dipole moment can be very large because each ferrofluid droplet contains many  $\text{Fe}_3\text{O}_4$  magnetite grains ( $\sim 1000$ ) and can be turned on with an externally applied magnetic field or turned off with removal of an externally applied magnetic field and the effects of thermal motion. These attributes make the ferrofluid droplets superparamagnetic, that is, their magnetic susceptibility is approximately 1.09 in SI units, which is five orders of magnitude larger than typical paramagnetic materials.

A single, isolated, magnetizable droplet of spherical shape will acquire a magnetic dipole moment,  $m$ , that is proportional to the externally applied magnetic field,  $H$ , as given by

the following expression, in SI units,

$$m = \mu_0 \left( \frac{4}{3} \pi a^3 \right) \chi H, \quad (1)$$

where  $\mu_0$  is the magnetic permeability of free space,  $a$  is the droplet radius, and  $\chi$  is the magnetic susceptibility of the droplet (as opposed to the bulk material). Two magnetized droplets with their magnetic dipole moments aligned along the magnetic-field direction will interact with each other through a potential energy,  $U_{d-d}$ , as given by the following expression, in SI units:

$$U_{d-d}(r, \theta) = \frac{m^2}{4\pi\mu_0} \left( \frac{1 - 3\cos^2\theta}{r^3} \right), \quad (2)$$

where  $r$  is the distance between the centers of the two droplets and  $\theta$  is the angle between the externally applied magnetic-field vector and the distance vector. The higher-order terms are negligible for the typical low magnetic field used in this study. If  $\theta$  is in the range of  $0^\circ < \theta < 55^\circ$  or  $125^\circ < \theta < 180^\circ$ , the droplets will attract one another, otherwise they will repel one another. If this dipole-dipole interaction energy is sufficiently strong, the droplets can acquire the unique and interesting property of linking together in a chainlike fashion. The formation of these chainlike structures is reversible when the externally applied magnetic field is removed. These chainlike structures, and more complex structures, have been studied in our earlier work [11,26,27].

The effective attraction or linkage of two ferrofluid droplets can be described by a coupling constant,  $\lambda$ , involving two competing factors: magnetic dipolar energy  $U_{d-d}$  and thermal energy  $k_B T$ . The dipolar magnetic energy aligns the droplets together while the thermal energy tries to randomize the droplets. The coupling constant  $\lambda$  is defined, in SI units, as

$$\lambda = \frac{U_{d-d}}{k_B T} = \frac{\pi\mu_0 a^3 \chi^2 H^2}{9k_B T}, \quad (3)$$

where the dipole-dipole interaction energy,  $U_{d-d}$  is calculated for two droplets that are nearly touching ( $r=2a$ ) and aligned head to tail ( $\theta=0$ ),  $k_B$  is the Boltzmann constant, and  $T$  is the temperature. The droplets are expected to form chains when  $\lambda \geq 1$ .

### III. EXPERIMENTAL SETUP AND PROCEDURES

In this study, light transmission, static light scattering, and optical microscopy are used to complement each other.

#### A. Light transmission

Figure 1 shows the light transmission experimental setup, which consists of a 10-mW He-Ne laser, a magnetic coil connected to a dc power supply, a glass sample cell, and a photodetector. The coil produces a magnetic field at a rate of 60 G/A at the coil's midsection along its axis. The sample is contained in a rectangular capillary cell of dimension 0.1 mm (inner thickness dimension)  $\times$  2 mm  $\times$  51 mm and sealed with petroleum jelly. The sample cell sits on top of a

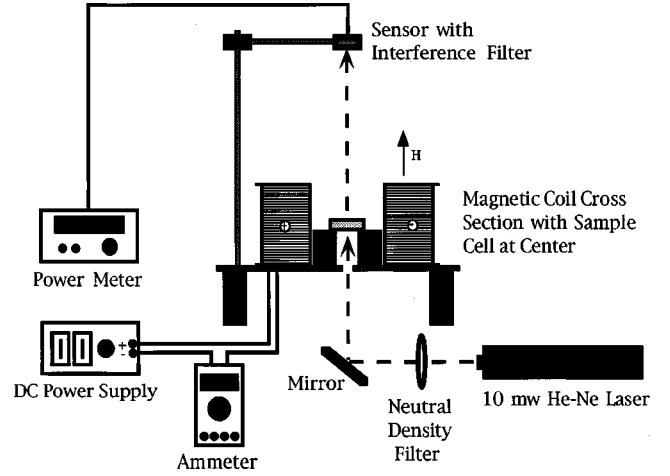


FIG. 1. Experimental setup for light transmission measurements.

hollow cylindrical mounting positioned inside the magnetic coil at the midsection of the coil. The laser beam, of wavelength 632.8 nm and approximate beam diameter 1.0 mm, is directed at the cell's surface along the coil's axis. Transmitted light is collected by a photodetector connected to a power meter. The photodetector has an aperture of approximately 1.0 cm in diameter and is positioned 42.5 cm above the center of the magnetic coil to avoid the first-order diffraction light and to reduce the small-angle light scattering through the sample cell to within a total angle of  $1.3^\circ$ . The power meter sensor is covered with a 632.8-nm interference filter, allowing only light with the wavelength of the laser beam to pass.

The incident light,  $I_0$ , is first measured without the sample in place. After the sample-filled cell is put inside the magnetic coil, the power supply current is then manually increased to generate the magnetic field at an average rate of 0.013 G/s, rising from 0 to 90 G or higher. The magnetic field specified throughout this paper is always an external magnetic field unless otherwise stated. This slow rate of change in the magnetic field is used so that an equilibrium state can be reached where the droplets have time to move in and out of the formed chains many times before the solid structures are formed. The intensity of the transmitted beam is then recorded as a function of the magnetic-field strength. The transmission is calculated by dividing the transmitted light intensity,  $I_t$ , by the incident light,  $I_0$ , and multiplying by 100.

#### B. Static light scattering

Static light scattering is used to verify results obtained from the light transmission measurements. Static light scattering measures the forward scattering pattern by using the same experimental setup as the light transmission experiment except that a white screen is used in place of the photodetector to display the scattering pattern. The scattering pattern is then observed with the naked eye and recorded by a CCD camera, connected to a VCR, positioned directly above the screen. Two experimental geometries are used to perform static light scattering. The first geometry has the laser beam perpendicular to the magnetic field by using a pair of mag-

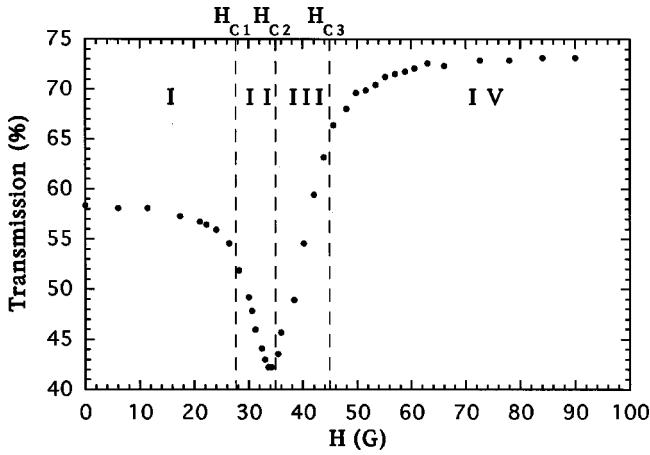


FIG. 2. Light transmission measurement showing structural transitions for  $\phi=0.9\%$  and cell thickness  $L=100\ \mu\text{m}$ . Four structural regimes are defined by three structural transition magnetic fields:  $H_{C1}$ ,  $H_{C2}$ , and  $H_{C3}$ , as indicated by the dashed lines.

netic coils rotated  $90^\circ$  relative to the laser beam. The second geometry has the laser beam parallel to the magnetic field, which is the same as the light transmission experiment, as well as our earlier static light-scattering experiments performed for equilibrium structure studies [11,19,26]. Instead of a capillary cell, the sample is held by a flat glass cell, covered with a glass slide, sealed with grease, and placed into a cell holder clip. The flat glass cell is 4.5 cm long, 1.2 cm wide, and 0.1 cm thick with a  $100\ \mu\text{m} \pm 5\ \mu\text{m}$  trough cut into one face of the cell to contain the sample.

### C. Optical microscopy

An inverted Nikon microscope is used to directly observe what is physically happening to the emulsion when subjected to a magnetic field. A glass capillary cell is used with either square or rectangular cross-section area with an inner thickness dimension ranging from 20 to  $100\ \mu\text{m}$ . The structures can be viewed either normal to the magnetic-field direction, where two magnetic coils are attached to the sides of the sample platform, or parallel to the magnetic-field direction, where one coil sits on top of the platform around the sample. A CCD camera is connected to the microscope and to a VCR. The power supply current is automatically increased to generate a magnetic field at a rate of 0.014 G/s from 0 to 60.6 G. As the magnetic field is increased, images are recorded.

## IV. EXPERIMENTAL RESULTS AND DISCUSSION

A typical measurement of light transmission through the ferrofluid emulsion as a function of the magnetic field,  $H$ , is shown in Fig. 2 for particle volume fraction  $\phi=0.9\%$ . The laser beam is parallel to the direction of the magnetic field. As the magnetic field is applied and slowly increased, the transmitted light intensity,  $I_t$ , slowly decreases in intensity but then enters a region where the intensity rapidly decreases, tracing out a curve in the process, until a minimum intensity is reached, as shown in Fig. 2 ( $[(I_t/I_0) \times 100]$  versus  $H$ ). The curved region ( $0 \leq H \leq 34\ \text{G}$ ) was fit-

ted with an analytical function (combined linear and hyperbolic tangent functions) and the minimum of the second derivative of the fitted function was calculated, via Mathcad, to obtain the magnetic field at which the maximum curvature occurs ( $H_{C1}=27.7\ \text{G}$ ). We call  $H_{C1}$  the first structural transition magnetic field. Once past the curved region, a minimum intensity is reached that is immediately followed by a rapid but continuous increase in the intensity, indicating that we have a second significant structural transition. The magnetic field at the minimum intensity is chosen as the measure of this second significant structural transition ( $H_{C2}=34.8\ \text{G}$ ). As the magnetic field increases further, the intensity rapidly increases but then enters a region where the intensity rapidly levels off, tracing out another curve in the process, until the intensity enters a saturation region, as shown in Fig. 2. This second curved region ( $35 \leq H \leq 90\ \text{G}$ ) indicates that another significant structural transition has occurred in the emulsion. We analyze it in the same way as the first curved region and obtain the third structural transition magnetic field ( $H_{C3}=44.7\ \text{G}$ ). The corresponding coupling constants for these three magnetic fields  $\lambda_{C1}=2.42$ ,  $\lambda_{C2}=3.79$ , and  $\lambda_{C3}=6.16$ .

The transmitted light intensity is an indicator of the structures formed in the emulsion fluid and how they are changing. The three structural transition magnetic fields divide the light transmission curve into four structural regimes. With the aid of the optical microscope, we can observe the structures formed by the emulsion droplets in real space and thus understand the physical characteristics of each of the structural regimes. Figure 3 shows such corresponding structures for the particle volume fraction  $\phi=0.9\%$  under the same conditions that were used for obtaining the data shown in Fig. 2.

In regime I, where  $\lambda < 1$ , the droplets are randomly distributed in a gas structure as shown in Fig. 3(a) so that they scatter and absorb the incident light, giving rise to the low  $I_t$  relative to  $I_0$ . When  $\lambda \sim 1$ , any two droplets in contact may form a dimer, a two-droplet chain, that constantly breaks up and reforms again. As stated earlier, the coupling constant for the first structural transition for  $\phi=0.9\%$  was experimentally found to be  $\lambda_{C1}=2.42$ . This is twice the value of the coupling constant at which droplets begin to form dimers. This can be understood by the fact that most individual particles are not in contact. The distance between the particles for  $\phi=0.9\%$  requires a larger magnetic field and, hence, a larger  $\lambda$  for particles to attract each other and overcome thermal motion to form dimers.

In regime II, where  $\lambda$  increases further, both the average chain length and the number of chains increase while the number of single particles decreases, as shown in Fig. 3(b). Light transmission is sensitive to the amount of light being scattered by the sample, which is determined by the size, shape, and number of scatterers in the sample. As more droplets pair up and short chains form, the number of scatterers decreases but the scattering cross section increases leading to a decrease in the transmitted intensity,  $I_t$ . In particular, a chain of particles acts like a cylindrical scatterer. Since the Rayleigh-Gans scattering intensity for a cylindrical scatterer is proportional to its length  $l$  and radius  $r$  as  $l^2 r^4$  [28], the

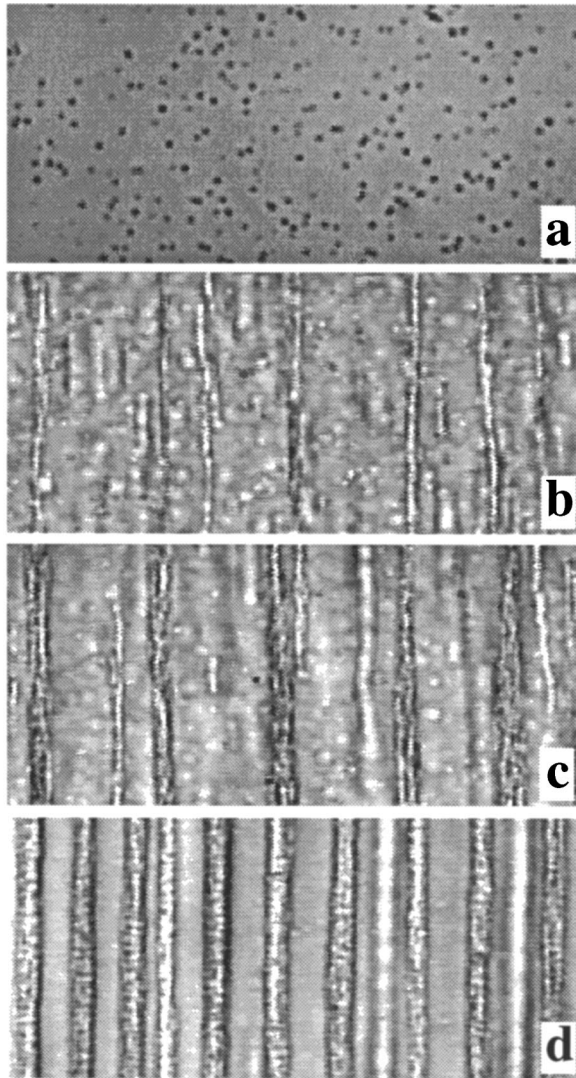


FIG. 3. Optical microscopic images showing structures at each of the four structural regimes in Fig. 2: (a) a gas structure at 15 G (regime I), (b) a coexistence of droplets and chains at 30 G (regime II), (c) a coexistence of droplets, chains, and columns at 42 G (regime III), and (d) a columnar solid structure at 60 G (regime IV). The horizontal width of each image is 40  $\mu\text{m}$ .

scattered light increases strongly as chains form. Furthermore, these chains are not rigid; they vibrate and fluctuate due to thermal motion [29]. Therefore, each chain acts as a cylindrical scatterer with an effective scattering radius  $r_{\text{eff}} \approx (la/\lambda)^{1/2}$ , which can be larger than  $a$ ; for example, with  $l = 20a$  and  $\lambda = 2$ , the effective scattering radius is  $r_{\text{eff}} \approx 3.2a$ . The strong scattering due to the growth of each chain and the vibration of long chains results in the further reduction in  $I_t$ , thereby leading to the observed dip in Fig. 2.

In regime III, the long chains reach nearly maximum length and they start to absorb neighboring short chains and single droplets, thereby forming columns as shown in Fig. 3(c). A depletion zone is created around the forming columns, which opens up the gap between the forming columns and reduces the number of scatterers, thereby increasing the light transmission.

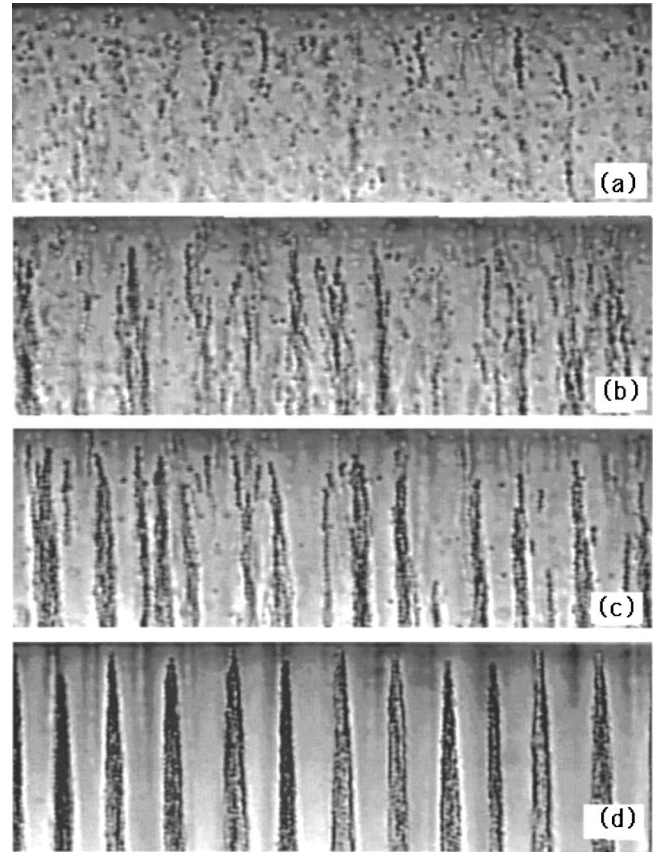


FIG. 4. Optical microscopic images showing the structural transitions from regimes II–IV for the experimental conditions of  $\phi = 3.0\%$ , particle diameter  $2a = 0.2 \mu\text{m}$ , and cell thickness  $L = 50 \mu\text{m}$ : (a) a coexistence of droplets and chains at 36 G, (b) a coexistence of droplets and chains at 42 G, (c) a coexistence of droplets, chains, and columns at 48 G, and (d) a columnar solid structure at 300 G. The horizontal width of each image is 60  $\mu\text{m}$ .

In regime IV, the columns are nearly equally spaced and they become more rigid with the droplets inside of them becoming more tightly packed with no single droplets or short chains remaining outside of the columns, as shown in Fig. 3(d). The light transmission then saturates with minimal change thereafter.

Figure 4 shows a better set of images of the same structural transitions from regimes II–IV near one end of the sample cell for a different set of experimental conditions:  $\phi = 3\%$ , particle diameter  $2a = 0.2 \mu\text{m}$ , and cell thickness  $L = 50 \mu\text{m}$ . Since the gaps between columns are generally much larger than the column width [11], more light is allowed to pass through. As a result, the saturated transmission intensity is always higher than the zero-field intensity. The same general behavior is observed for all of the particle volume fractions studied,  $0.3\% \leq \phi \leq 10\%$ , as shown in Fig. 5. It should be noted that data were also collected for the particle volume fractions of 12% and 14% but were not included in the analysis since our laboratory demonstrated that high concentrations are susceptible to the effects of multiple scattering at the early stage of chain formation, therefore the transmission may not reflect the structural transition accurately. In addition, Fig. 5 shows data up to 90 G, but data

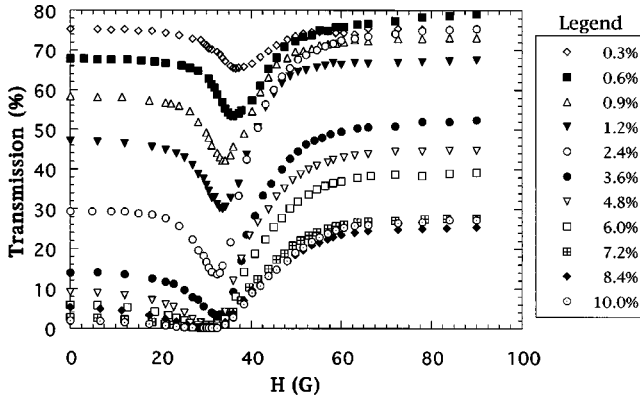


FIG. 5. Composite light transmission measurements for all particle volume fractions studied ( $0.3\% \leq \phi \leq 10\%$ ).

were collected up to as high as 360 G for some of the particle volume fractions. Since these data points occurred in the saturation region and remained fairly steady, they were not included in the figure.

The structure of droplets in regime I clearly corresponds to a gas structure. The structure of regime II is similar to that of molecular liquid crystals, with all the chains parallel to the magnetic-field direction but with random positions and chain length. This structure may be called “nematic-liquid-crystal-like.” As seen from Fig. 3(b) and Figs. 4(a) and 4(b), gas and liquid coexist in this regime. As the magnetic field increases, separate thin columns are formed with a few chains loosely bound within each column, as shown in Fig. 4(c). Since the particle density inside a thin column is less than the close-packing density, this structure may be called a columnar liquid. As a result, the structure in regime III may be described as a coexistence of gas, “nematic-liquid-crystal-like,” and columnar liquid. Finally, the rigid columns in regime IV correspond to a solid structure.

In order to quantitatively understand the characteristic magnetic fields measured in Fig. 2, we use small-angle light scattering to measure the threshold magnetic fields in two geometries for  $\phi=0.9\%$ . In the first geometry, the incident light beam is perpendicular to the magnetic field so that the scattering pattern is sensitive to the chaining of the droplets. As  $H$  increases, an anisotropic ellipsoidal scattering pattern becomes visible at 27.1 G that evolves into a bright narrow band that is perpendicular to both the magnetic field and the incident light beam. This band indicates that anisotropic scatterers are forming parallel to the magnetic-field direction. The magnetic field at the onset of the anisotropic pattern is comparable to the magnetic field determined by light transmission for the first structural transition for  $\phi=0.9\%$  ( $H_{C1} = 27.7$  G). This provides supporting evidence for our use of the minimum of the second derivative of the fitted curve in determining the first structural transition magnetic field.

In the second geometry, the incident light is parallel to the magnetic-field direction so that the scattering pattern is sensitive to the structures of the scatterers in the plane perpendicular to the magnetic field, that is, it is sensitive to the formation of columns. When the magnetic field increases to  $H'_{C2} = 33.6$  G [Fig. 6(a)], the scattering light intensity starts to increase beyond the background noise. As the magnetic

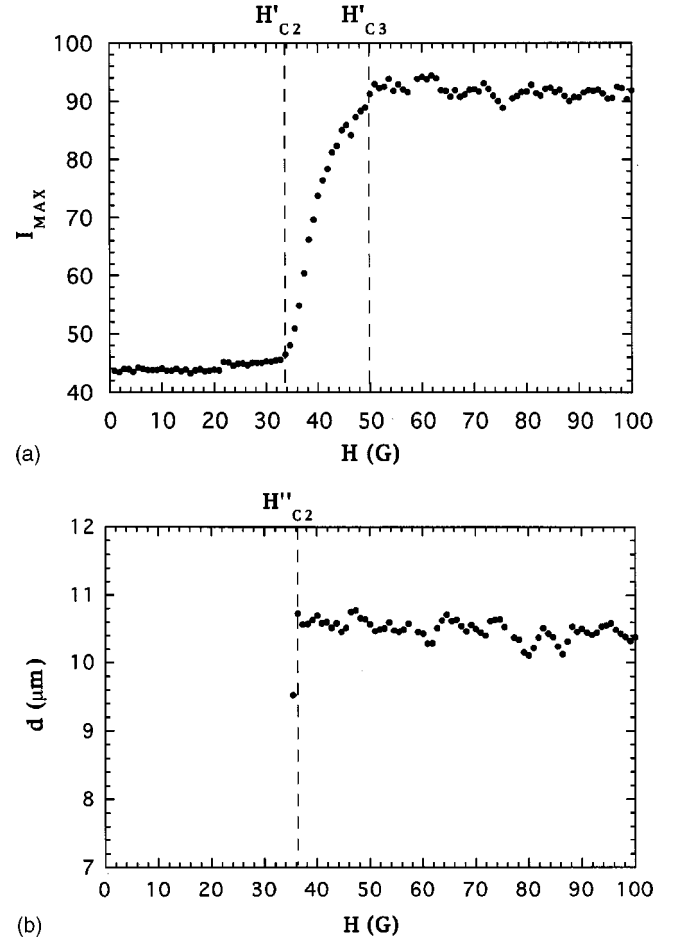


FIG. 6. (a) Peak intensity of scattered light as a function of the magnetic field for  $\phi=0.9\%$  and cell thickness  $L=100 \mu\text{m}$ . (b) Static light-scattering measurement showing average column spacing as a function of the magnetic field for the same data set as in (a). Here the light is parallel to the magnetic-field direction and  $d$  is defined as  $2\pi/q_{\text{max}}$ , where  $q_{\text{max}}$  is the first ring peak position. No ring peak is observed until magnetic field reaches 36.3 G.

field increases further to  $H''_{C2} = 36.3$  G [Fig. 6(b)], a ring appears in the scattering pattern. The ring becomes sharper as the magnetic field increases further and the peak intensity saturates at  $H'_{C3} = 50.0$  G [Fig. 6(a)]. Figure 6(b) shows the ring peak position  $d$  obtained from  $q_{\text{max}}$ , the scattering wave vector at the maximum intensity,  $I_{\text{max}}$ . The ring peak intensity measures the ordering of the columns in the  $x$ - $y$  plane normal to the magnetic-field direction, whereas the ring peak position measures the average column separation,  $d = 2\pi/q_{\text{max}}$  [11]. At  $H''_{C2}$ , the centers of the columns are very well defined and column separation does not change with further increases in  $H$ , although the column width may still change (decrease when the columns tighten) and the ordering may still increase. As a result, the structural transition from single chains to thin columns ( $H_{C2}$ ) must fall within the range  $H'_{C2} < H_{C2} < H''_{C2}$ . The value for  $H_{C2}$  (34.8 G) falls within the expected range confirming that the light transmission measurements provide a good indication of the second structural transition. At  $H'_{C3}$ , the ordering among columns reaches a maximum, giving rise to the saturation of  $I_{\text{max}}$ . The

TABLE I. Structural transition magnetic fields ( $H_{C1}, H_{C2}, H_{C3}$ ), for each particle volume fraction, and their corresponding coupling constants ( $\lambda_{C1}, \lambda_{C2}, \lambda_{C3}$ ).

Volume fraction (%)	$H_{C1}$ (G)	$H_{C2}$ (G)	$H_{C3}$ (G)	$\lambda_{C1}$	$\lambda_{C2}$	$\lambda_{C3}$
0.3	29.1	36.9	47.7	2.67	4.25	6.97
0.6	30.1	36.6	48.4	2.85	4.18	7.17
0.9	27.7	34.8	44.7	2.42	3.79	6.16
1.2	27.0	33.9	44.2	2.30	3.60	6.03
2.4	25.4	32.7	43.6	2.04	3.36	5.87
3.6	24.2	32.7	44.6	1.86	3.36	6.13
4.8	20.4	31.8	43.4	1.32	3.18	5.82
6.0	18.8	31.2	46.2	1.13	3.06	6.56
7.2	14.4	31.5	47.6	0.662	3.12	6.95
8.4	15.5	30.9	49.2	0.767	3.00	7.40
10.0	13.2	30.9	50.3	0.557	3.00	7.72

magnetic field  $H'_{C3}$  is greater than the magnetic field determined by light transmission for the third structural transition for  $\phi=0.9\%$ ,  $H_{C3}=44.7\text{G}$ . This is to be expected since  $H'_{C3}$  measures the end of the solid structural formation with tightened chains within the columns, while  $H_{C3}$  measures the beginning of the solid structural formation with loose chains within the columns.

The light-scattering results are consistent with the light transmission measurements showing that the light transmission measurements can be used to investigate structural transitions. For particle volume fractions higher than 5% and cell thickness  $100\ \mu\text{m}$ , the light-scattering technique is limited by the occurrence of multiple light scattering, especially at the early stage of chain formation. Therefore, light transmission makes possible the extension of the range of measurements to higher particle volume fractions as long as the particle volume fractions are not too high ( $>10\%$ ).

We repeated the light transmission measurements for particle volume fractions,  $\phi$ , ranging from 0.3% to 10% and obtained similar results, as shown in Fig. 5. We used the same analysis methods for each of these light transmission measurements as were used for the  $\phi=0.9\%$  light transmission measurement (Fig. 2) and obtained three corresponding structural transition magnetic fields,  $H_C$ , for each  $\phi$ , as shown in Table I.

Table I shows that  $\lambda_{C1} < 1$  when  $\phi \geq 7.2\%$  for the first structural transition. This may be due to the polydispersity of particles in our sample and the definition of  $\lambda$  used. The values in Table I are based upon the average particle size, but larger size particles can still form chains since their magnetic interaction energy may be larger than  $k_B T$  even though  $\lambda_{C1} < 1$ . In addition, the local magnetic field inside a particle within a chain is larger than the magnetic field inside a single particle alone due to the reduced demagnetization field from the chain geometry, thereby increasing the effective coupling constant further.

The structural transition magnetic fields in Table I were used to construct a structural transition diagram, as shown in Fig. 7. The solid lines in Fig. 7 are theoretical fits of the three

structural transition magnetic fields which are discussed further in Sec. V.

It is interesting to notice that in Fig. 4(d) the end shape of each column in the solid structure is tapered and the columns are quite regularly separated. The end shape is not limited to tapering only. Figure 8 shows that the tapered ends [Figs. 8(a) and 8(c)], at the low particle volume fraction of  $\phi = 3\%$  and particle diameter  $2a = 0.5\ \mu\text{m}$ , can be changed to split ends [Figs. 8(b) and 8(d)] at the higher particle volume

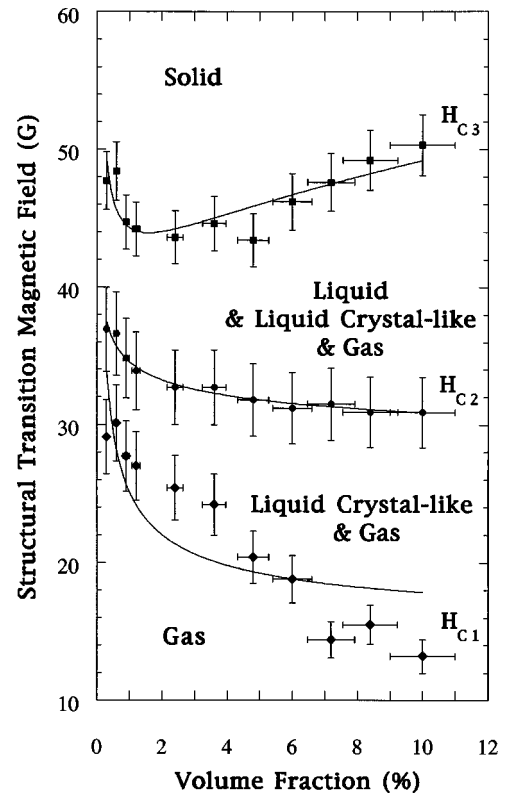


FIG. 7. Structural transition diagram for the ferrofluid emulsion. The solid lines are theoretical fits of the three structural transition magnetic fields.

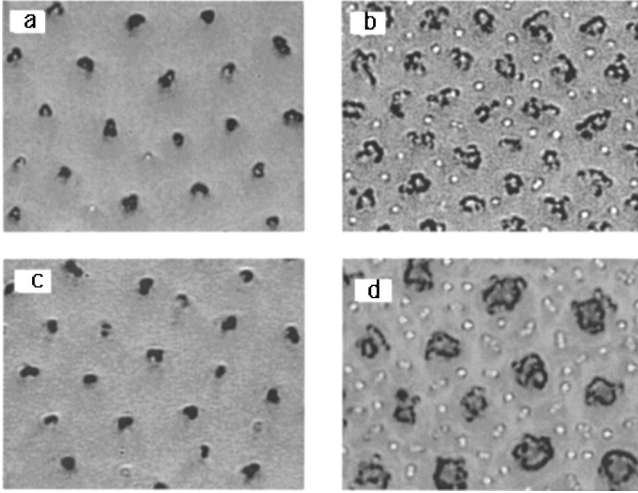


FIG. 8. Optical microscopic images showing the shapes of the ends of the columns in the solid structure for ferrofluid emulsion of particle diameter  $2a=0.5\ \mu\text{m}$ . Tapered ends are seen for  $\phi=3.0\%$  and (a)  $L=20\ \mu\text{m}$ , (c)  $L=50\ \mu\text{m}$ . Split ends are seen for  $\phi=10.0\%$  and (b)  $L=20\ \mu\text{m}$ , (d)  $L=50\ \mu\text{m}$ . The horizontal width of each image is  $27.5\ \mu\text{m}$ .

fraction of  $\phi=10\%$ , while keeping the same cell thickness  $L=20\ \mu\text{m}$  [Figs. 8(a) (tapered) and 8(b) (split)] and  $L=50\ \mu\text{m}$  [Figs. 8(c) (tapered) and 8(d) (split)] along the magnetic-field direction. Notice that the shape of split ends becomes more connected and bigger when cell thickness increases from 20 to  $50\ \mu\text{m}$  as shown in Figs. 8(b) and 8(d). If we keep the cell thickness at  $L=20\ \mu\text{m}$  and move from the tip of the column up toward its center, the split ends [Fig. 9(a) at  $\phi=10\%$ ] and tapered ends [Fig. 9(c) at  $\phi=3\%$ ] at the very tip of the column will become disklike with a wider cross section only  $6\ \mu\text{m}$  [Fig. 9(b) at  $\phi=10\%$ ] and  $5\ \mu\text{m}$

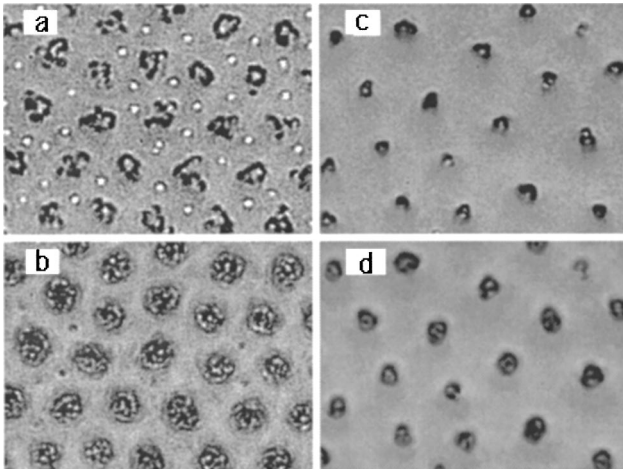


FIG. 9. Optical microscopic images showing different cross sections of the columns for  $2a=0.5\ \mu\text{m}$  and  $L=20\ \mu\text{m}$ . In (a) and (b),  $\phi=10.0\%$  and images are taken at the very tip of the column (a) and  $6\ \mu\text{m}$  up from one end of the column (b). In (c) and (d),  $\phi=3.0\%$  and images are taken at the very tip of the column (c) and  $5\ \mu\text{m}$  up from one end of the column (d). The horizontal width of each image is  $25\ \mu\text{m}$ .

[Fig. 9(d) at  $\phi=3\%$ ] away from the tip. Therefore, the end shape holds for only a short distance.

These end shapes of solid structure and the regular separation between columns are due to the fact that structural growth within the ferrofluid emulsion is confined by the walls of the sample cell. The confinement causes the columns to terminate with an effective magnetic charge at both ends due to the packing of magnetic dipoles in the droplets. Image dipoles do not exist due to the use of a magnetic coil, which is different from what is used for ER fluids. All of the columns have the same signed effective magnetic charges at the top of the sample cell and the same opposite-signed effective magnetic charges at the bottom of the sample cell. This causes the ends of neighboring chains within each column to repel each other. Minimizing the repulsive energy results in shifting neighboring chain positions along the magnetic-field direction as shown in our earlier computer simulation [30]. If one chain in a thin column reaches the boundary of the sample cell, the rest of the chains try to move away from the boundary, thereby forming a tapered column. If a thicker column has a large number of chains, the shifting of neighboring chains can go in both directions ( $+z$  or  $-z$ ) along the radius of the column, where chains with the same length try to stay away from each other resulting in split end shapes. Since the column width increases with both the particle volume fraction and the cell thickness, as our earlier work has shown [11,26], the tapered ends for thin columns change to split ends for thicker columns as both  $L$  and  $\phi$  increase.

The magnetic charges at the ends of the columns also cause neighboring columns to repel one another. This results in local ordering of columns and further coalescence between the columns is not possible. This monopole repulsion between columns is important in the equilibrium structure formation, as our earlier work has shown [11,26]. It is also an important factor in determining  $H_{C2}$ , as shown in our theoretical model below.

## V. THEORETICAL MODELS

In order to understand the structural transitions and their associated magnetic fields, theoretical models were derived to provide the relationships between the three structural transition magnetic fields and the particle volume fractions. All the calculations are in Gaussian units.

The first structural transition magnetic field,  $H_{C1}$ , decreases with the particle volume fraction,  $\phi$ . We believe that this can be understood simply from the competition between the dipolar interaction energy of two droplets,  $U_{d-d}$ , and the thermal energy,  $k_B T$ . The dipole-dipole interaction is a long-ranged interaction that favors chain formation while the thermal energy favors randomizing chains and droplets. The interaction energy is built up as the magnetic field increases and magnetic dipoles are induced in the droplets. When  $U_{d-d} > k_B T$ , two droplets are able to form a dimer chain. These dimers are not permanent. They constantly break up into individual droplets and recombine into dimers. The number and lifetime of dimers increases as the average droplet separation  $d$  decreases or as the particle volume fraction

increases. Therefore, the condition for the first structural transition magnetic field,  $H_{C1}$ , is

$$\frac{2(m)^2}{d^3} = k_B T, \quad (4)$$

where  $m = \beta a^3 H$  is the magnetic dipole moment,  $\beta = (\mu_p - \mu_f)/(\mu_p + 2\mu_f)$ , with  $\mu_f$  and  $\mu_p$  the permeability of the solvent and the ferrofluid, respectively,  $H$  is the magnetic field, and  $d$  is the average droplet separation. Once some of the larger droplets form chains first, the chains may attract smaller droplets and grow.

Using  $\phi \approx (4\pi/3)(a/d)^3$  with  $a$  the average droplet radius, and assuming a uniform distribution of particles in the sample cell, we obtain the relationship between the first structural transition magnetic field,  $H_{C1}$ , and the particle volume fraction,  $\phi$ ,

$$H_{C1} \approx \frac{1}{\beta} \left( \frac{2\pi k_B T}{3a^3} \right)^{1/2} \phi^{-1/2}. \quad (5)$$

Using  $\mu_p = 2.7$  for the ferrofluid and  $\mu_f = 1$  for water (which gives  $\beta = 0.36$ ),  $a = 0.15 \mu\text{m}$ , and  $T = 300 \text{ K}$ , we fitted Eq. (5) to the experimental data, as shown in Fig. 7. The fitting is qualitative rather than quantitative as we have allowed the fitting to have multiplicative and offset coefficients to account for the approximate nature of Eq. (5). The theoretical model did capture the decreasing trend of the first structural transition magnetic field. It can be seen from Fig. 7 that the lower particle volume fractions tend to be above the fitting while the higher particle volume fractions tend to be below the fitting, in particular for  $\phi \geq 7.2\%$ . In the case of the lower particle volume fractions, the average particle separation is quite large so that the chains end up forming when  $\lambda > 1$ . As  $\phi$  increases, the distances between the particles become smaller, therefore a smaller magnetic field and a smaller  $\lambda$  will be required to attract droplets and form chains. Hence, a decreasing function of  $H_{C1}$  is to be expected.

The second structural transition magnetic field,  $H_{C2}$ , corresponds to the formation of long chains that serve as the nucleation centers of columns. It is experimentally observed that column formation is initiated by the long chains serving as nucleation centers, which attract neighboring short chains and single droplets to form columns [31]. These nucleation centers have an average spacing, but weak local ordering, perpendicular to the direction of the magnetic field. As the magnetic field increases, these nucleation columns attract additional individual droplets and chains causing the columns to grow larger and to develop an increased local ordering. This local ordering is caused by a repulsive Coulomb interaction,  $U_q$ , between the effective magnetic charges  $q_m$  at the ends of neighboring columns, as indicated by the end shapes shown in Figs. 8 and 9.  $U_q$  favors the ordering of the long chains, whereas the thermal energy tends to destroy the local order. We believe that the competition between these two energies sets the second structural transition magnetic field. As the particle volume fraction increases, the neighboring long chains become closer and the interaction between them

gets stronger. Therefore, a large  $\phi$  implies that a lower magnetic field is required to form columns.

The repulsive Coulomb interaction energy between two neighboring columns is

$$U_q \approx \frac{q_m^2}{\rho}. \quad (6)$$

The condition for the second structural transition magnetic field,  $H_{C2}$ , is therefore given by

$$\frac{q_m^2}{\rho} \approx k_B T, \quad (7)$$

where  $q_m \propto \beta a^2 H$  and  $\rho$  is the average separation distance between the columns. This relation is valid if the length of the columns is much larger than the separation between the columns, which is the case in our experiment.

If we assume that the columns are very thin at this stage, the particle volume fraction  $\phi$  can be approximated as

$$\phi \propto (a/\rho)^2. \quad (8)$$

Combining Eqs. (7) and (8), we obtain the relationship between the second structural transition magnetic field,  $H_{C2}$ , and the particle volume fraction  $\phi$ ,

$$H_{C2} \propto \frac{1}{\beta} \left( \frac{k_B T}{a^3} \right)^{1/2} \phi^{-1/4}. \quad (9)$$

Using experimental conditions, we fitted Eq. (9) to the experimental data, as shown in Fig. 7. The fitting is qualitative rather than quantitative as we have allowed the fitting to have multiplicative and offset coefficients to account for the approximate nature of Eq. (9).

For a small sample cell thickness, for example 10–20  $\mu\text{m}$ , the repulsive Coulomb interaction energy [Eq. (6)] has to be modified by including higher-order terms for the next-nearest neighbors, which leads to the relation  $H_{C2} \propto \phi^{-x}$ , where the exponent  $x$  should be greater than 0.25 but smaller than 0.75. This scaling analysis is consistent with the experimental data from Hwang and Wu that  $x = 0.5$  for the second structural transition magnetic field,  $H_{C2}$  [17].

Previously, we used a different condition for the second structural transition magnetic field by balancing the attractive energy between long chains with neighboring short chains and the thermal energy [19]. Even though the result also shows the same  $\phi$  dependence, it is not clear that the direct interaction can be neglected in the column formation. When considering the experimental result from Hwang and Wu for shorter chains [17], the physical picture used here seems more appropriate.

The third structural transition magnetic field,  $H_{C3}$ , is different from the first and second structural transition magnetic fields in that the corresponding structural transition occurs inside the individual columns. Specifically, it is a transition from liquidlike loosely bound chains to solidlike densely packed columns. In the structural regime just below  $H_{C3}$ , the structures consist of single chains and columns where the columns consist of chains that are liquidlike and fluctuate

due to thermal motion. In the structural regime above  $H_{C3}$ , the structures are solid columns where the droplets that had comprised the chains have been rearranged to be close-packed and may well have the body-centered-tetragonal (BCT) structure [14]. There is no longer a one-dimensional characteristic of chains within the individual columns. In the transition, the short-range direct interaction energy is a binding energy for making the columns rigid, while the fluctuation of chains due to Peierls-Laudau instability has the opposite effect. We believe that competition of these two energies sets the third structural transition magnetic field.

The attractive short-range direct interaction energy is [7,8]

$$U_i = \left(\frac{m^2}{a^3}\right) \pi^2 \left(\frac{2a}{\rho}\right)^{1/2} \cos(z\pi/a) \exp\left(-\frac{\pi\rho}{a}\right), \quad (10)$$

where  $z$  is the distance in the direction of the magnetic field. The fluctuation energy for a single chain of the droplets in a column [31] is

$$U_f \approx m \left(\frac{27\pi}{128}\right)^{1/2} \left(\frac{a^2 k_B T}{\rho^5}\right)^{1/2}. \quad (11)$$

Equating Eq. (10) and Eq. (11) results in a relation for the third structural transition magnetic field,  $H_{C3}$ ,

$$H_{C3} \approx \left(\frac{27\pi k_B T}{256a^3}\right)^{1/2} \left(\frac{1}{\beta\pi^2}\right) \frac{1}{|\langle \cos(z\pi/a) \rangle|} \left(\frac{a}{\rho}\right)^2 \exp\left(\pi\frac{\rho}{a}\right), \quad (12)$$

where  $\rho$  is the separation between the chains in a column.

The fluctuation energy can be attractive especially at larger chain separations, where it is proposed to be the main driving force for chain aggregation [32]. In the case where the chain separation is short, the attractive short-range direct interaction dominates the fluctuation attractive energy. Therefore, it is the direct interaction energy that is important and competes with the repulsive fluctuation energy to set the third structural transition magnetic field.

In the structural regime just below  $H_{C3}$ , if we assume uniform liquid-crystal-like structures where the chains within the columns form local hexagonal structures, we have

$$\left(\frac{a}{\rho}\right)^2 \approx \frac{\phi^1}{(1.21)^2}. \quad (13)$$

In the structural regime above  $H_{C3}$ , if we assume BCT solidlike structures [14] such that  $(a/\rho)$  is a constant, we have

$$\left(\frac{a}{\rho}\right)^2 \approx \frac{\phi^0}{(1.73)^2}. \quad (14)$$

At the structural transition magnetic field, we may assume that the following general relationship exists:

$$\left(\frac{a}{\rho}\right)^2 \approx \frac{\phi^\gamma}{G^2}, \quad (15)$$

where  $\gamma$  reflects the sensitivity of the particle volume fraction dependence of the average distance between the chains within the columns ( $0 \leq \gamma \leq 1$ ) and  $G$  is a geometric factor reflecting the chain structure within the columns.

Using Eq. (15), Eq. (12) becomes

$$H_{C3} \approx \left(\frac{27\pi k_B T}{256a^3}\right)^{1/2} \left(\frac{1}{\beta\pi^2}\right) \frac{1}{|\langle \cos(z\pi/a) \rangle|} \left(\frac{\phi^\gamma}{G^2}\right) \exp\left(\frac{\pi G}{\phi^{(\gamma/2)}}\right). \quad (16)$$

In Eq. (16), we may set  $|\langle \cos(\pi z/a) \rangle| = 0.65$  based upon the following argument: for a monodisperse sample, the position of droplet number  $j$  in a straight chain is  $z = (2j + 1)a$ , which gives  $\cos(\pi z/a) = -1$ . Since our sample has 35% polydispersity, the average position of droplet number  $j$  in a chain deviates from its perfect position by 35%, therefore  $\cos(\pi z/a) = -0.65$  and  $|\langle \cos(\pi z/a) \rangle| = 0.65$ .

Using the experimental conditions, we fitted Eq. (16) to the experimental data, as shown in Fig. 7. The fitting is qualitative rather than quantitative, as we have allowed the fitting to have a multiplicative coefficient to account for the approximate nature of Eq. (16). The fit of Eq. (16) gives us  $\gamma = 0.39$ , which falls within our expected range, and  $G = 0.29$ , which indicates that the particles are not uniformly distributed throughout the columns. From the agreement between the calculation and the experimental result for  $H_{C3}$ , we see that the short-range direct interaction plays a key role in the formation of the columnar solid structure. This is consistent with the ground-state calculations of others for dipolar fluid [7,8].

When  $\phi$  increases, the column separation is constant but the column width in steady state increases, as was shown in our earlier work [11], therefore the magnetic field required to tighten more chains in a column should also increase. This may account for the rise of  $H_{C3}$  in Fig. 7.

## VI. CONCLUSION

A ferrofluid emulsion exhibits complex structures with the application of a slowly increasing magnetic field. The detailed study shows that structural transition, from initial gas to final solid, consists of two regimes of coexistence of structures instead of just one, as found in isotropic colloids such as hard spheres and charged colloids. As the magnetic field increases, a total of four structural regimes is observed: (I) randomly dispersed droplets (gas), (II) individual droplets (gas) and chains (“nematic-liquid-crystal-like”) coexistence, (III) individual droplets (gas), chains (“nematic-liquid-crystal-like”), and loosely bound columns (liquid) coexistence, and (IV) tightly bound columns (solid).

Three structural transition magnetic fields are measured with the light transmission experiment as a function of particle volume fraction. A structural transition diagram is constructed. Our theoretical models fit the experimental data

well for the second and third structural transition magnetic fields and qualitatively show the decreasing trend for the first structural transition magnetic field. From this, we find the driving force to be the dipole-dipole interaction between droplets in the first structural transition, the repulsion between magnetic charges at the ends of long chains defines the center of columns in the second structural transition, and the direct chain-chain interaction is responsible for the binding of chains to form solid columns in the third structural transition.

The monopole repulsion between the ends of chains within a column causes the ends of the column to be tapered

at low particle volume fractions and split ends at higher particle volume fractions.

#### ACKNOWLEDGMENTS

We wish to thank the following individuals for their contributions and assistance in making this research possible: K. Javier, J. Pousset, P. Sheaffer, G. Flores, Dr. J. Bibette, Professor R. Sheng, Dr. G. Hu, Dr. M. Gross, Dr. M. Hangenbuehle, Dr. R. Tao, and Dr. T. Halsey. This work was partially supported by NSF Grant No. DMR 9321201, NASA (NAG3-1830), the Research Corporation, and CSULB University Research.

- 
- [1] P. N. Pusey and W. van Megen, *Nature (London)* **320**, 340 (1986).
- [2] R. Crandall and R. Williams, *Science* **198**, 293 (1977).
- [3] D. A. Weitz and M. Oliveria, *Phys. Rev. Lett.* **52**, 1433 (1984).
- [4] S. E. Paulin and B. J. Ackerson, *Phys. Rev. Lett.* **64**, 2663 (1990).
- [5] *Proceedings of the 5th International Conference on Electro-Rheological Fluids, Magneto-Rheological Suspensions and Associated Technology, Sheffield, UK, 1995*, edited by W. Bullough (World Scientific, Singapore, 1996).
- [6] *Proceedings of the 6th International Conference on Electro-Rheological Fluids, Magneto-Rheological Suspensions and their Applications, Yonezawa, Japan, 1997*, edited by M. Nakano and K. Koyama (World Scientific, Singapore, 1998).
- [7] T. C. Halsey and W. Toor, *Phys. Rev. Lett.* **65**, 2820 (1990).
- [8] R. Tao and J. M. Sun, *Phys. Rev. Lett.* **67**, 398 (1991).
- [9] E. Lemaire, Y. Grasselli, and G. Bossis, *J. Phys. II* **2**, 359 (1992).
- [10] Y. Grasselli, G. Bossis, and E. Lemaire, *J. Phys. II* **4**, 253 (1994).
- [11] J. Liu *et al.*, *Phys. Rev. Lett.* **74**, 2828 (1995).
- [12] K. Sano and M. Doi, *J. Phys. Soc. Jpn.* **52**, 2810 (1983).
- [13] R. Tao, *Phys. Rev. E* **47**, 423 (1993).
- [14] R. Tao and Q. Jiang, *Phys. Rev. Lett.* **73**, 205 (1994).
- [15] T-j. Chen, R. N. Zitter, and R. Tao, *Phys. Rev. Lett.* **68**, 2555 (1992).
- [16] M. Fermigier and A. P. Gast, *J. Colloid Interface Sci.* **154**, 522 (1992).
- [17] Y. H. Hwang and X.-I. Wu, *Phys. Rev. E* **49**, 3102 (1994).
- [18] S. Cutillas, G. Bossis, E. Lemaire, A. Meunier, and A. Cebers, *Ref. [6]*, p. 149.
- [19] Y. Zhu, M. L. Ivey, P. Sheaffer, J. Pousset, and Jing Liu, *Int. J. Mod. Phys. B* **10**, 2973 (1996).
- [20] J. Bibette, *J. Magn. Magn. Mater.* **122**, 37 (1993).
- [21] J. Bibette, *J. Colloid Interface Sci.* **147**, 474 (1991).
- [22] F. L. Calderon, T. Stora, O. Mondain, M. P. Poulin, and J. Bibette, *Phys. Rev. Lett.* **22**, 2959 (1994).
- [23] P. M. Sheaffer, M.S. thesis, California State University, Long Beach, 1995.
- [24] J. Bibette, D. C. Morse, T. A. Witten, and D. A. Weitz, *Phys. Rev. Lett.* **69**, 2439 (1992).
- [25] T. G. Mason, Ph.D. dissertation, Princeton University, 1995.
- [26] E. M. Lawrence, M. L. Ivey, G. A. Flores, J. Liu, J. Bibette, and J. Richard, *Int. J. Mod. Phys. B* **8**, 2765 (1994).
- [27] G. A. Flores, M. L. Ivey, J. Liu, M. Mohebi, and N. Jamasbi, *Int. J. Mod. Phys. B* **10**, 3283 (1996).
- [28] H. C. van de Hulst, *Light Scattering by Small Particles* (Dover, New York, 1981).
- [29] S. Cutillas and J. Liu, *Phys. Rev. E* (to be published).
- [30] M. Mohebi, N. Jamasbi, and Jing Liu, *Phys. Rev. E* **54**, 5407 (1996).
- [31] Y. Zhu, E. Haddadian, T. Mou, M. Gross, and J. Liu, *Phys. Rev. E* **53**, 1753 (1996).
- [32] T. C. Halsey and W. Toor, *J. Stat. Phys.* **61**, 1257 (1990).